



Contents lists available at ScienceDirect

Journal of Power Sources

journal homepage: www.elsevier.com/locate/jpowsour



Review

In situ microscopic studies on the structural and chemical behaviors of lithium-ion battery materials



Minhua Shao*

Department of Chemical and Biomolecular Engineering, The Hong Kong University of Science and Technology, Clear Water Bay, Kowloon, Hong Kong

HIGHLIGHTS

- Microstructural evolution and state-of-charge mapping in LIB materials.
- Microscopic techniques development and applications in the study of LIBs.
- Review and discussion of limitations and advantages of each microscopic technique.

ARTICLE INFO

Article history:

Received 9 May 2014

Received in revised form

14 July 2014

Accepted 20 July 2014

Available online 8 August 2014

Keywords:

Microscopic techniques

Silicon

Lithium-ion battery

State-of-charge

Structural evolution

ABSTRACT

The direct observation of the microstructural evolution and state-of-charge (SOC) distribution in active materials is crucial to understand the lithiation/delithiation mechanisms during electrochemical cycling of lithium-ion batteries (LIBs). Owing to their high spatial resolutions and capability to map chemical states by combining other spectroscopic techniques, microscopic techniques including X-ray fluorescence (XRF) microscopy, Raman microscopy, transmission X-ray microscopy (TXM), scanning electron microscopy (SEM), and transmission electron microscopy (TEM) play significant roles in real time monitoring the dynamic changes in the LIB electrodes and materials. This paper reviews the recent progress of using *in situ* microscopic techniques to study LIB materials, including Si-, Sn-, Ge-, C- and metal oxides-based anode materials, and layered oxysulfide, metal fluorides, LiCoO₂, LiNi_{0.8}Co_{0.15}Al_{0.05}O₂, LiMn₂O₄, LiFePO₄ cathode materials.

© 2014 Elsevier B.V. All rights reserved.

1. Introduction

The widespread use of electrified vehicles (EVs) demands energy storage devices with high specific energy capacities. Compared with other energy storage devices, the lithium-ion battery (LIB) is one of the most promising choices even though it has several significant issues, including safety, low specific and volumetric capacities, slow charge/discharge rates, and high cost [1–4]. Recent work focuses on the development of advanced anode and cathode materials for high energy and power density LIBs to meet the requirement of EVs [5–7]. The direct observation of the structural evolution and chemical state changes of the active materials during the cycling of LIBs is essential to understand the lithiation/delithiation mechanisms and eventually help design better batteries. There has been growing interest in developing various spectroscopic and microscopic techniques in order to *in situ*

monitor the dynamic electrochemical process in LIBs. These techniques include but are not limited to infrared spectroscopy [8], X-ray diffraction (XRD) spectroscopy [9–11], Raman spectroscopy [12,13], nuclear magnetic resonance (NMR) spectroscopy [14,15], X-ray fluorescence (XRF) microscopy [16], Raman microscopy [17], transmission X-ray microscopy (TXM) [18], scanning electron microscopy (SEM) [19], transmission electron microscopy (TEM) [20,21], and scanning probe microscopy (SPM) [22,23]. Recent results from these studies have significantly advanced the understanding of the physical and chemical behaviors of electrodes and individual particles during electrochemical cycling. Some of the advantages and disadvantages of each technique have been discussed in recent papers [20,21,24]. This review focuses on the recent results (mostly since 2010) obtained by *in situ* microscopic techniques, including XRF microscopy, Raman microscopy, TXM, SEM, and TEM. The purpose of this survey is to summarize the current development of these techniques and their applications in the study of LIB materials. The limitations, strengths, and future applications of each technique are discussed.

* Tel.: +852 3469 2269; fax: +852 2358 0054.

E-mail addresses: Kemshao@ust.hk, minhua@gmail.com.

2. Microscopic studies on LIB materials

2.1. X-ray fluorescence microscopy

XRF spectrometry has been widely used in the areas of industrial minerals, geological and climate change, forensics, biology, etc., due to its element specific capability [25]. By fast scanning the sample through an X-ray beam, the elemental distribution maps of the sample can be generated. The μm -scale spatial resolution of this imaging technique, however, is relatively too low for the study of most battery materials. Due to this reason, its application in the study of a working LIB did not take place until recently when Robert et al. [16] successfully used a synchrotron-based XRF imaging technique to investigate the structural behavior of a layered oxy-sulfide $\text{Sr}_2\text{MnO}_2\text{Cu}_{3.5}\text{S}_3$ during electrochemical reaction with Li. It is known that the layered oxy-sulfide consists of alternating $[\text{Sr}_2\text{MnO}_2]$ and $[\text{Cu}_2\text{S}]$ sheets [26]. The reaction mechanism of $\text{Sr}_2\text{MnO}_2\text{Cu}_{3.5}\text{S}_3$ with Li involves the displacement of Cu, which is different from the classic intercalation pathway. During lithiation of $\text{Sr}_2\text{MnO}_2\text{Cu}_{3.5}\text{S}_3$, the Li atom can insert itself into the framework and replace the Cu atom resulting in the extrusion of metallic Cu [26,27]. By coupling with XAS and XRD, the authors were able to monitor the shape change of the particles and oxidation states of the elements by following the individual particles with the XRF imaging at the different stages of lithiation. It was found that the extrusion of Cu was reversible and the microstructure of $\text{Sr}_2\text{MnO}_2\text{Cu}_{3.5}\text{S}_3$ did not change during the lithiation/delithiation process [16]. As mentioned, due to the low spatial resolution of this technique, its application in the study of LIB materials is very limited.

2.2. Raman microscopy

Raman spectroscopy is also suitable for characterizing the physicochemical properties of the electrolyte/electrode interface due to its surface sensitivity and relatively high spatial resolution (up to hundreds of nm) [28]. The potential of Raman microscopy to generate local surface composition images and

state-of-charge (SOC) maps for composite electrodes or monitor in real time the spectroscopic behavior of several individual particles in composite cathodes during a charge/discharge cycle has already been demonstrated.

Pantiz and Novák [29] firstly explored the feasibility of using Raman spectroscopy to map the SOC of LiCoO_2 electrodes with a spatial resolution of a few μm . The position, width, and intensity ratio of the Raman bands can be used as descriptors of SOC distribution. The Raman active ($A_{1g} + E_g$) modes of LiCoO_2 correspond to oxygen vibrations in directions parallel (A_{1g}) or perpendicular (E_g) to the c -axis. These modes are sensitive to the presence of Li atoms in the layered rock-salt lattice. As shown in Fig. 1b, the frequency of the A_{1g} band shifts to higher wavenumbers during discharge (increase in the Li content of the LiCoO_2 lattice) [17]. The Raman spectra change as a function of the SOC which enables the distribution of the local SOC to be obtained by constructing Raman images of the A_{1g} peak positions. The broadening of the SOC distribution in Fig. 1b indicates various discharge rates of individual LiCoO_2 particles and inhomogeneous current distribution within the electrode, which is confirmed by the Raman images during charge/discharge shown in Fig. 1a [17]. Some particles (red and yellow arrows) were charged and discharged at a slower rate during the 1st cycle. Part of them became irreversibly charged during the 2nd cycle. A few particles (blue arrows) were charged and discharged at a fast rate during the 1st cycle, but at a much slower rate during the 2nd cycle. The percentage of the fully charged LiCoO_2 particles at the end of the 2nd discharge was 6% higher than that at the end of the 1st discharge (16% vs. 10%). The increase of the number of inactive particles was caused by an increase in the electrical resistance between LiCoO_2 particles.

$\text{LiNi}_{0.8}\text{Co}_{0.15}\text{Al}_{0.05}\text{O}_2$ (NCA) also has a layered structure similar to that of LiCoO_2 . Thus, its Raman spectra follow the same trend when the SOC changes. Lei et al. [30] found that the charge/discharge rates of individual NCA particles in a tested LIB vary significantly with time and location due to the local degradation of the conducting matrix. A Raman mapping study further revealed that the carbon matrix providing the electrical conductive path between the NCA particle agglomerates and the current collector, and between

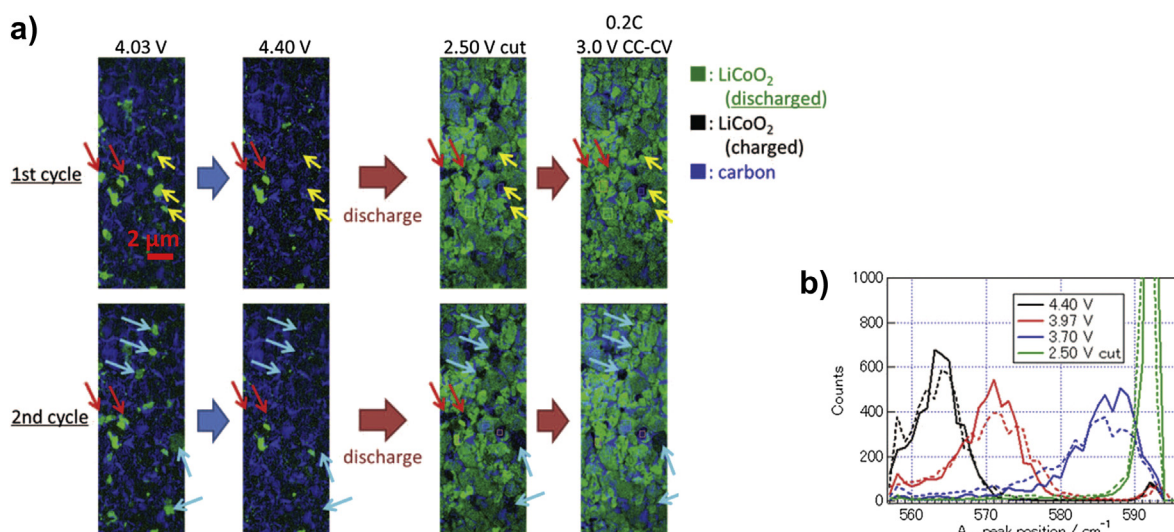


Fig. 1. (a) Comparisons of the Raman images acquired during the 1st and 2nd charge (0.4 C)/discharge (1 C followed by 0.2 C) cycles of LiCoO_2 . In the discharge process, the cell voltage relaxed from 2.5 to 3.7 V after galvanostatic discharge to 2.5 V at 1 C rate. The cell was additionally discharged at a slower rate (0.2 C) to 3.0 V followed by potentiostatic discharge at 3.0 V for 3 h. The red arrows: particles that were charged and discharged at a slower rate during both the 1st and 2nd cycles; The yellow arrows: particles that were charged at a slower rate in the 1st charge process and then became irreversibly charged; The blue arrows: particles that were charged and discharged at a normal rate during the 1st cycle but at a slower rate during the 2nd cycle. (b) A_{1g} peak position of LiCoO_2 as a function of electrode potential during the 1st (solid) and 2nd (dashed) discharge processes [17]. (For interpretation of the references to color in this figure legend, the reader is referred to the web version of this article.)

the individual particles in the agglomerates degrades after cell testing [31,32]. The carbon redistribution/retreat is possibly caused by carbon gasification, SEI layer formation, loss of physical adhesion, mechanical rearrangement, and electrophoretic transport of carbon particles resulting in loss of the electrical conductive path through the degraded carbon matrix. As a consequence, the resistance within and between agglomerates increases. In the worst case, some oxide particles are totally isolated and become inactive. The inhomogeneous distribution of SOC of an aged electrode containing NCA particles was also observed by Nanda et al. by Raman mapping [33].

The inhomogeneous local distribution of SOC in LCO and NCA electrodes is responsible for the uneven performance of the cathode. Some areas of the electrode are charged and discharged at a higher rate than the average current, which may lead to local overcharge or overdischarge. This can cause structural instability, metal dissolution, and oxygen release of the active materials and contribute to the degradation of the electrode performance during further cycling.

In the case of LiMn_2O_4 (LMO) with a spinel structure, the position of its Raman band at $\sim 592 \text{ cm}^{-1}$ (Eu mode) does not shift upon charge/discharge. In contrast, the band becomes broader from $\lambda\text{-MnO}_2$ to $\text{Li}_x\text{Mn}_2\text{O}_4$ during discharge [34]. The shape and intensity changes of the Raman band are caused by the alternation of the electronic properties of the electrode by lattice expansion upon Li^+ insertion. In this case, the statistical analysis of LMO Raman spectra is more complicated than that of materials with a layered structure. Classical least squares (CLS) and multivariate curve resolution (MCR) methods have been used to deconvolute the Raman spectra in order to obtain the contributions from fully discharged (LiMn_2O_4), half discharged ($\text{Li}_{0.5}\text{Mn}_2\text{O}_4$), and fully charged ($\lambda\text{-MnO}_2$) [34]. The SOC as a function of applied potential can be roughly derived from these approaches during reduction of $\lambda\text{-MnO}_2$. Compared with the SOC plot extracted from the coulometric analysis of the electrode, the former shifts along the potential axis by $\sim 40 \text{ mV}$ in a positive direction [34]. Note that the SOC obtained from the Raman spectra and voltammetric scan is based on the surface and bulk regions, respectively. The potential lag in the coulometric analysis suggests that the surface region probed by Raman reaches equilibrium with the applied potential much faster than the rest of the oxide, i.e., it takes much longer to reach equilibrium for the entire oxide due to the Li^+ diffusion within the lattice.

Raman microscopy is a powerful tool to characterize the SOC at the electrode level but not within the individual particles due to its sub-micro spatial resolution. It is particularly useful to investigate in real time the inhomogeneous SOC distributions in the electrodes containing layered oxide materials.

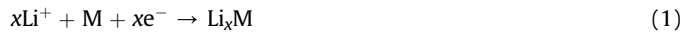
2.3. Scanning transmission X-ray microscopy

In a STXM, a thin section of a specimen is raster-scanned in a focused X-ray beam and an image is generated by monitoring the X-ray signal transmitted through the specimen. TXM has a spatial resolution of sub 30 nm, which is one order of magnitude higher than Raman microscopy. The resolution is high enough for the study of LIB materials since their particle sizes typically range from hundreds of nanometers to a few microns [24,35–40]. More and more studies on the morphological changes and SOC mapping using STXM have been carried out.

2.3.1. Morphology evolution

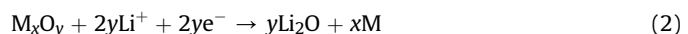
TXM is well suited to the study of the lithiation/delithiation process involving large volume changes. Li-alloying materials (M),

such as Sn, Si, Al, and Mg, can alloy with Li during the lithiation following the reversible alloying reaction:



The lithiation process of Sn-based anode materials including Sn alloys and pure Sn particles have been investigated by Chao et al. [18,41]. The lithiation rate of smaller Sn particles ($<4 \mu\text{m}$) is much faster than that of larger ones [41]. In the former, homogeneous lithiation was observed without cracking, while a core–shell type structure formed in the latter with severe cracking in the Li_xSn phase during the first lithiation, suggesting the interfacial conversion reaction rather than the Li^+ diffusion was the rate determining step in the alloying process. The much faster lithiation rate in the smaller particles can be explained by the core–shell kinetics model, in which the time required to achieve the same lithiation rate is proportional to the square of particles' diameter. In contrast, the size dependence was not observed for the SnSb alloy particles [18]. Sb in SnSb alloy can easily form a porous Li_3Sb surface layer at potentials around 0.8 V, which is higher than the lithiation potential of Sn (0.37 V). The ready formation of a porous layer enables fast lithiation of all particles regardless of their size.

In the case of some metal oxides, pure metal is formed in the first lithiation process together with inactive Li_2O :



The metal rather than the metal oxides undergoes the consequent lithiation-delithiation process. Using *in situ* TXM, Chao et al. [42] found that a porous Li_2O matrix serving as the backbone was firstly formed during the first lithiation of a SnO secondary particle consisting of plates of primary particles. Then the lithiation occurred on the precipitated Sn nanoparticles. Compared with the dense Sn microparticles, the SnO anode material possesses much faster lithiation/delithiation kinetics, lower volume expansion, and better mechanical integrity due to the formation of small Sn particles and Li_2O backbones. Another metal oxide studied was CuO particles [43]. A size-dependent and core–shell kinetics model was revealed. An interphase mainly consisting of Cu_2O was observed between the CuO core and Cu shell in large particles during the first few lithiation/delithiation cycles.

With advanced Fresnel zone plates, it is possible to achieve spatial resolutions below 10 nm for TXM [44,45]. Clearer subtle morphological and structural changes can be observed with the newly developed TXM.

2.3.2. State-of-charge mapping

By combining with X-ray absorption spectroscopy (XAS), which is sensitive to the chemical states of elements, STXM can be used to map the chemical states of the studied materials at a very high resolution, which is only limited by the size of the focused spot of the X-ray (10–40 nm). Lithium intercalation and phase transformation in LiFePO_4 (LFP) particles in a real battery environment is still a topic of debate. At a constant current, it is still not clear whether intercalation occurs in all the LFP particles concurrently or via a particle-by-particle pathway. In the latter, only a fraction of the particles undergoes phase transformation at a given time resulting in the situation that most of the particles in the electrode are either Li-rich or Li-poor during lithiation/delithiation. Synchrotron-based STXM combined with XAS was used to image the local SOC distribution in multiple LFP particles in a half-charged electrode [46]. A change in the oxidation state of Fe atoms from 2^+ to 3^+ resulted in an absorption energy shift of 2 eV (from 708 to 710 eV) during delithiation of LFP enabling the determination of Fe species in the XAS spectra. As shown in Fig. 2, about 65%

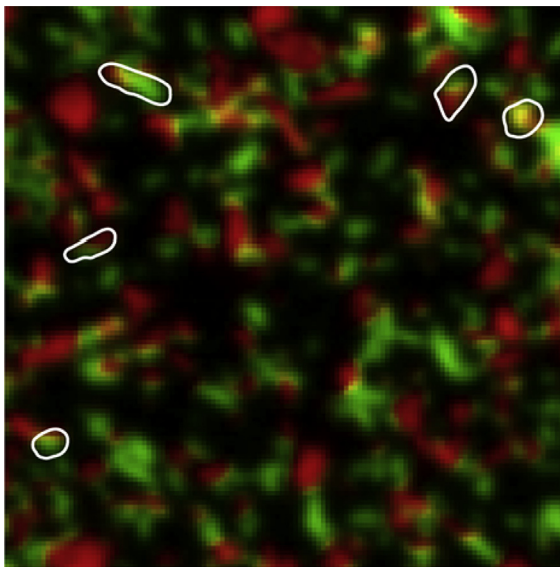


Fig. 2. State-of-charge mapping obtained via scanning transmission X-ray microscopy in the LFP composite electrode with 50% state-of-charge. Red, green and yellow represent Li-rich (>85%), Li-poor (<15%) and mixed particles. The particles in white cycles are actively undergoing delithiation [46]. (For interpretation of the references to color in this figure legend, the reader is referred to the web version of this article.)

(delithiated) and 32% (lithiated) of the particles were Li-poor (green) and Li-rich (red), respectively. Only less than 3% (yellow particles circled in Fig. 2) of the particles were actively undergoing delithiation when the charge process was terminated. This result confirms that the particle-to-particle pathway dominates in the delithiation process in LFP electrodes [46]. It also implied that the time for charging a LFP particle is about 50 times faster than that for the whole electrode. The state-of-charge mapping results clearly reveal that the rate determining step in charging the LFP particles is the initial nucleation of the phase transformation. Once initiated, the rate of the remaining phase transformation is relatively fast. In addition, the kinetics of the nucleation of the phase transformation do not depend on the particle size, i.e., the phase transformation does not necessarily occur and complete first on the small particles.

The detailed mechanism of the phase transformation in a single LFP particle, however, is still unclear. It is well-known that the most favorable lithium diffusion path is through 1D tunnels aligned with the *b*-axis [47,48]. The *ex situ* STEM-EELS study suggests the phase transition occurs by a successive emptying of the Li^+ channels along the *b*-axis [47]. This process results in a core of FePO_4 surrounded by a shell of LiFePO_4 . A recent *ex situ* STXM and TXM study clearly showed that the delithiation of the LFP is more favorable at the edge than at the center of the particle [49]. However, this does not exclude the possibility that the delithiation at the edge and in the center start at the same time. The further progress of the delithiation at the center may be interfered with by the defects (voids and cracks), which are mainly present at the center of the crystal.

STXM can also be used in the study of the possible strong chemical interaction between cathode active materials and carbon (acting as the conductive medium). By mapping the Fe valance state of the $\text{LiMn}_{0.75}\text{Fe}_{0.25}\text{PO}_4$ (LMFP) nanorods–graphene hybrid nanostructure, the local SOC status can be revealed [50]. By combining the local C K-edge XAS, the SOC status and the P–O–C interaction strength can be correlated. The stronger the P–O–C interaction, the higher the SOC. This result suggests that the hybrid electrode benefits from the strong interaction between LMFP and graphene [50], which is essential for the high-rate performance in lithium-ion batteries.

STXM has become more popular in the study of LIB materials due to its unique properties: low damage to the materials caused by the beam exposure, high spatial resolution, flexible electrochemical cell setup, and its ability to identify chemical states with the assistance of XAS. However, this technique requires a synchrotron light source thereby preventing it from being used by most researchers.

2.4. Scanning electron microscopy

The high spatial resolution of scanning electron microscopy (SEM) enables it to be a very powerful tool for *in situ* and *ex situ* characterization of materials at the nanoscale. It has been widely used to study the structure of electrode materials of LIBs. Most of the time, the pristine or tested electrode materials harvested from the batteries after testing are *ex situ* characterized by SEM [51]. Due to the high vacuum needed in the SEM chamber, the residues of the electrolytes have to be removed before SEM measurements. Extreme care has to be taken to avoid material contamination and exposure to air/moisture during the cell dismantling and electrode cleaning. Attempts to develop an *in situ* SEM technique to investigate working LIBs have been made. The first was by Baudry and Armand [52]. In their approach, a polymeric electrolyte without severe evaporation was used but the cell was exposed to the air before being transferred into the SEM chamber. The common electrolytes, ethylene carbonate (EC) and dimethyl carbonate (DMC), were used in Orsini et al.'s study, in which the electrolytes were frozen at -20°C before being transferred to the SEM chamber without exposure to the air [53]. In this approach, however, electrochemical cycling could not take place inside of the SEM chamber and the measurements had to be taken quickly. Environmental scanning electron microscopy (ESEM), which is tolerant to high vapor pressure, was also applied in the study of Sn electrodes using solvents like ethylene and propylene carbonate (PC). Chen et al. [19] used a room temperature ionic liquid (IL) butylmethylpyrrolidinium–TFSI (BMPyr–TFSI) based electrolyte in a standard SEM. Ionic liquids exhibit extremely low vapor pressures and hence can be used under ultra-high vacuum conditions. They developed a sample transfer process without exposing the battery cell to the air. Electrochemical cycling could be performed inside of the SEM chamber by connecting the cell through the micromanipulator and the SEM sample stub, as shown in Fig. 3.

Using this setup, Chen et al. [19] found that the small SnO_2 particles in the order of 100 nm form a continuous Li_2O layer completely encapsulating the particles during lithiation. The

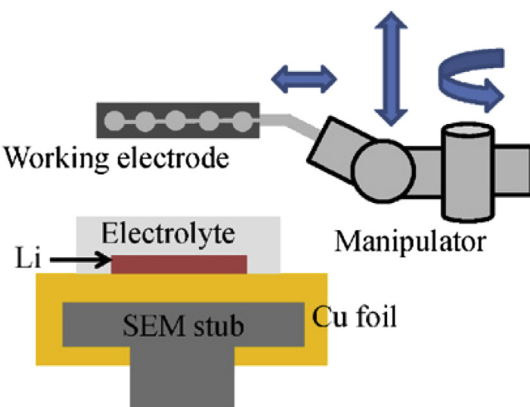


Fig. 3. Illustration of an *in situ* SEM electrochemical cell. The working electrode placed on the separator was pressed on the Li metal sheet in the ionic liquid electrolyte by a manipulator [19].

observation of the formation of a Li_2O layer is consistent with the *in situ* STXM study conducted by Chao et al. [42]. The irreversible volume expansion of the particle occurred within the first few lithiation/delithiation cycles. No cracking or pulverization was observed in such small particles in the charge/discharge process indicating the excellent structural stability of this core–shell type composite. On the other hand, the large particles (~500 nm in this study) responded to the insertion of Li in a totally different way. Besides the volume increase, cracks and extrusions occurred frequently on the large particles even after the first insertion of Li, as shown in Fig. 4. No Li_2O surface layer was observed. The extrusions, which may consist of Sn or Sn–Li alloy, only formed and grew during Li insertion. The formation and growth mechanisms of the extrusions are not clear. Nevertheless, the formation of the extrusions and cracks on the larger particles implies inhomogeneous chemical reactions with Li.

The behavior of large SnO_2 particles during lithiation/delithiation in the SEM study was different from that seen in the STXM experiment discussed in Section 2.3. In the latter, a porous Li_2O matrix formed during the first lithiation of a SnO particle. Besides different types of oxides (SnO_2 vs. SnO) used in these studies, there are other factors which may contribute to their different behaviors. One is the electrolytes used. 0.5 M of Li–bis(trifluoromethanesulfonyl)imide (Li–TFSI) in BMPyrr–TFSI ionic liquid and 1 M of LiPF_6 in EC + ethyl methyl carbonate (EMC) were used in the SEM and STXM experiments, respectively. The reaction mechanisms with Li in different electrolytes are likely different for Sn oxides. The other factor may be due to the spatial resolutions of the instrument. The typical resolution of a STXM is about 30 nm, which is lower than that of SEM (down to a few nm in the *in situ* measurements). The subtle changes (cracks and extrusions) on the individual nanoparticles may be difficult to be captured by STXM due to its lower spatial resolution.

2.5. Transmission electron microscopy

It is a dream for battery scientists to observe in real time the structural and morphological changes of active materials at the atomic level during charge/discharge. TEM, due to its subnanometer spatial resolution, has been extensively applied in material characterizations. The direct imaging of atomic columns of light elements, such as Li, with atomic resolution in real time remains a great challenge [54–60]. In the past, the observation of the structural and chemical evolution of battery materials has mostly relied on *ex situ* studies [61,62], which may lack dynamic information and in some cases is even misleading. Many efforts have

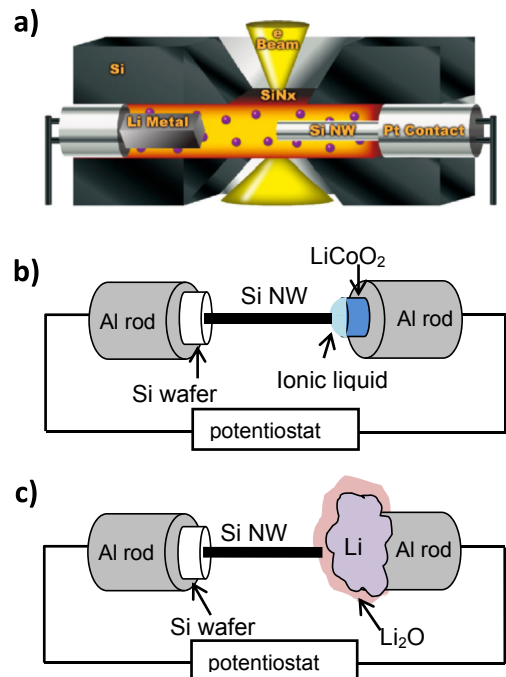


Fig. 5. Schematic drawing showing the experimental setup of the closed-cell battery (a), and open-cell approach using ionic liquid (b) and Li_2O grown on metallic Li as electrolytes (c). Adapted from Refs. [21,63].

been made to develop an *in situ* TEM technique to study battery materials. The major technical hurdle is to introduce a proper electrolyte into the TEM column with a typical vacuum level at 10^{-5} Pa. The typical liquid electrolytes used in LIBs, such as PC and DME, have a high vapor pressure and cannot be used directly in the TEM column. Currently, there are three approaches to mitigate this issue. The first is to use a closed cell design in which a thin liquid electrolyte layer is sealed in a microcell by extra-thin electron transparent SiN_x membranes, as illustrated in Fig. 5a [63,64]. The advantage of this approach is that the structural and chemical evolution of the battery materials is close to that of those in a real LIB since battery relevant electrolytes are used. The spatial resolution, however, is limited by the liquid electrolyte layer. In addition, the potential leakage and evaporation of electrolytes puts the high vacuum TEM column in danger. The second approach is to use an open cell design. Two types of open cell designs have been

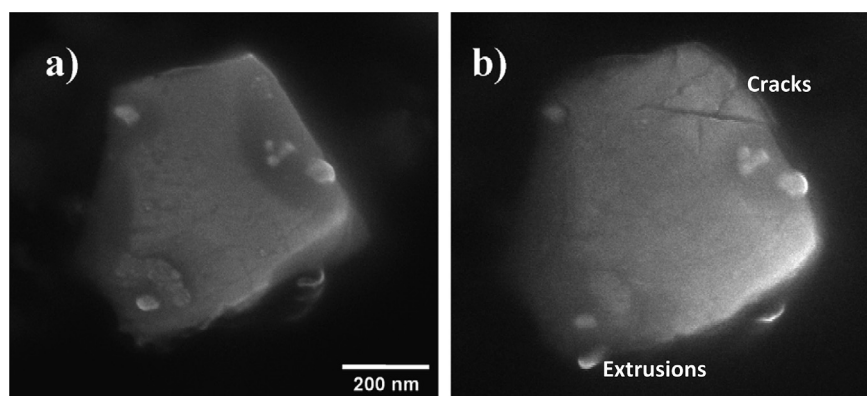


Fig. 4. A single SnO_2 particle before (a) and after the first lithium insertion (b). Besides the volume expansion, cracks and extrusions appeared on the particle surface after the first lithium insertion [19].

developed. In one of the designs, ionic liquid electrolytes (ILEs), which have an extremely low vapor pressure, are dropped onto a LiCoO₂ cathode, as shown in Fig. 5b [20,21]. The other design (Fig. 5c) uses a thin Li₂O layer as a solid electrolyte, which is readily formed on metallic Li when it is exposed to air for a very short period (a few seconds). In both cases, the materials to be investigated (nanostructures or bulk films) are attached to a conductive substrate and brought into contact with the electrolytes (ionic liquid or Li₂O layer) by a piezo-positioner at fine steps to form nanobatteries. The advantage of the open cell is that it allows recording of microstructure changes in real time and at atomic-scale resolution, and concurrent nanometer to atomic-scale composition analysis during lithiation/delithiation [20,21]. However, it also has shortcomings. The electrolytes are only in point contact with the electrode, which may inadvertently modify the diffusion pattern of Li in the electrode (though the full immersion of the electrode in the ILE was demonstrated recently [65], the interaction between the electrode and ILEs may not be the same as for the real electrolytes used in LIBs). In addition, some unique phenomena occurring in real battery electrolytes may be missed in ionic liquid and Li₂O solid electrolytes. Regardless of the deficiencies of the current approaches, they provide insightful information regarding the structural and chemical evolution of electrodes at unprecedented spatial resolution by other microscopic techniques upon lithiation/delithiation.

2.5.1. Lithiation/delithiation in anode materials

2.5.1.1. Si and Ge. Si and Ge are both promising candidates to replace graphite as anode materials for LIBs due to their high volumetric and gravimetric capacities. The volumetric capacities of Si and Ge are 8344 Ah L⁻¹ for Li₁₅Si₄ and 7366 Ah L⁻¹ for Li₁₅Ge₄, respectively. The gravimetric capacities are 3579 mAh g⁻¹_{Si} and 1384 mAh g⁻¹_{Ge}, respectively [7,66–68]. However, the significant volume change during cycling (~300%) in Si and Ge-based materials results in damage to the integrity of the active materials and electrodes. This causes practical challenges in regard to their applications in LIBs. In order to develop a robust anode electrode containing Si and Ge, further understanding of the lithiation/delithiation processes and their effects on the structural changes of various Si and Ge nanostructures is required. *In situ* TEM techniques have been developed and applied in these studies.

Liu et al. [69] found that the <112>-oriented Si nanowire exhibits a dumbbell-shaped cross-section after lithiation in *in situ* TEM studies using open-cell nanobatteries. The unique dumbbell-shape as shown in Fig. 6a with larger swelling along the radial <110> direction than the <111> direction is caused by orientation-dependent Li insertion rates, which are much faster along the [110] direction than the [111] direction. As a result, the diameter of the nanowire increases by over 200% along the <110> direction, but the length increases by less than 10% along the <111> direction. The difference in Li insertion rate among crystalline orientations is consistent with the density functional theory (DFT) calculation results which show that the onset lithiation potential of the Si(110) plane is generally higher than that of other low index planes [70]. The faster reaction along the <110> direction causes a larger stress along the same direction than that along the <111> direction. The larger stress in turn enhances the Li diffusion rate. Thus the coupling effect between the diffusion anisotropy and stress leads to the formation of the dumbbell-shaped structure after lithiation. The anisotropic expansion of Si nanowires and nanopillars were also observed in *ex situ* and *operando* TEM experiments using a closed-cell nanobattery [63]. The anisotropic volume expansion suggests that the lithiation kinetics of Si nanostructures are determined by the reaction rate at the interface rather than by the diffusion of Li through the lithiated phase.

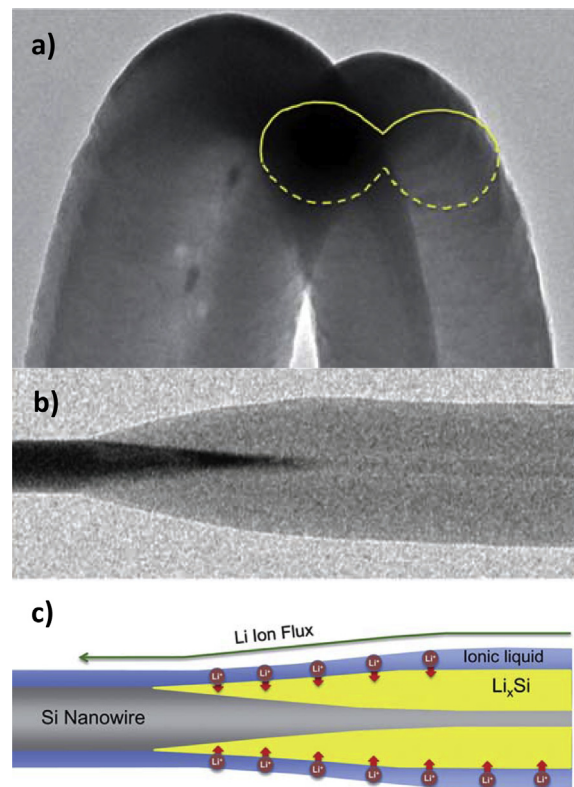


Fig. 6. *In situ* TEM image of a bent lithiated <112>-oriented Si NW showing a dumbbell cross-section (a) [69]. *In situ* TEM image of a Si NW during lithiation (b) and illustration of Li diffusion along the surface and insertion into the Si NW (c) [73].

During lithiation of a Si nanowire, a core–shell structure consisting of a crystalline (c-Si) core and an amorphous (*a*-Li_xSi alloy) ($x \approx 3.75$) formed as Li was continuously inserted into the nanowire, as shown in Fig. 6. Once the Li/Si molar ratio reached 3.75, the amorphous shell suddenly crystallized into Li₁₅Si₄, consistent with previous findings and DFT calculation results [71]. As Wang et al. [72] observed in an *in situ* TEM study, the crystallization occurs through the fast propagation of the interface between the crystallized region and the amorphous region along the Li⁺ diffusion direction. The crystallization and lithiation front propagation speeds were comparable (~130 nm s⁻¹) [72]. Li et al. [69] found that even after prolonged lithiation, the pure c-Si core still exists. The incomplete lithiation of the Si core indicates that the lithiation rate of Si nanowire is very slow due to its extremely low electrical conductivity. Various approaches such as doping, coatings, and nanocomposites have been applied to improve the charge/discharge rates of Si electrodes. It has been demonstrated that P-doping and C-coating can improve the charge rate of Si nanowires by one order of magnitude due to the dramatic increase in electrical conductivity [73–77]. The *in situ* TEM results reveal that the carbon coating does not suppress the radial expansion but improves the flexibility of the brittle Si nanowires. Depending on the thickness of the carbon coating, it might maintain its intact structure (<10 nm) or break into pieces (>10 nm) during the first cycle. These results suggest that a thinner carbon coating is desirable to maintain the structural integrity of the core–shell structure [73].

On the other hand, *a*-Si can also be coated on carbonaceous materials, such as carbon nanofibers (CNFs), forming a nanocomposite. The combination of the high stability of CNF and gravimetric capacity of Si makes the Si/CNF nanocomposite a promising anode material. In an *in situ* TEM study, Wang et al. [72]

found that the *a*-Si layer is strongly bonded to the CNF and no cracking/fracture is observed during the first few cycles. Later, a sandwich-like lithiation mechanism was found by another group. In the early stage of lithiation, most of the Si–C bonds at the interface break followed by the formation of Li–C bonds. The modification of the interface properties makes it a fast Li⁺ transport channel. Thus lithiation is able to occur from both the top and bottom surface of the Si layer [78].

Karki et al. [79] found an interesting welding process between two physically contacted Si nanowires during lithiation/delithiation cycling. As Li reacts with Si, the Si–Si binding energy decreases dramatically from 2.72 eV to 0.08 eV. When the surfaces of the two Si nanowires come into contact, Li atoms readily bond with Si atoms at the interface of the two Si nanowires. During delithiation, the dangling Si bonds formed by the broken Si–Li–Si are forced to bond to one another at the interface in order to lower the free energy of the system. The strength of the interfacial weld between two Si nanowires was measured to be ~200 MPa, which is comparable to that of stainless steel. The strong welding phenomenon between active materials can guide the design of robust electrode architecture, which can significantly mitigate the capacity fade caused by the fracture and detachment from the current collector.

Similar to Sn particles discussed in Section 2.3, Si particles also show particle size dependent lithiation behavior [68,80]. *In situ* TEM experiments with a solid electrolyte configuration demonstrate that cracks appear on large *c*-Si particles during lithiation but

not on smaller ones [81]. The critical diameters were determined to be about 150 nm for nanoparticles by Liu et al. [81] and 240–360 nm for nanopillars by Lee et al. [62]. The crack always initiates in the surface of the amorphous *a*-Li_xSi shell rather than in the *c*-Si core, and propagates inward quickly as the lithiation continues, leading to pulverization of the particle, as shown in Fig. 7A. The stress analysis model demonstrates that the surface fracture and its propagation into the core are caused by the large tensile hoop stress that is reversed from the initial compression stress in the surface layer of the *a*-Li_xSi shell, as shown in the inset of Fig. 7A [81]. Unlike the large particles, the Si particles less than 150 nm are much more robust and no cracking is observed during lithiation. As shown in Fig. 7B, the thickness of the *a*-Li_xSi shell gradually increases as the lithiation progresses and a uniform Li₁₅Si₄ structure is achieved after full lithiation. The anisotropic expansion observed in the Si nanowires also occurs in the *c*-Si particles. It is suggested that the tensile hoop stress in the smaller particles is not large enough to drive the initiation and consequent propagation of surface fracture [81]. It is worth noting that the critical particle size depends on the lithiation rate. The faster the reaction rate, the more the fractures in the surface. This could be caused by the fact that there is not enough time to relax the large tensile hoop stress in the surface when the reaction rate is fast. McDowell et al. [82] studied the lithiation/delithiation behaviors of an amorphous Si (*a*-Si) sphere using the same technique and found some interesting aspects that were different from the *c*-Si sphere. There was no

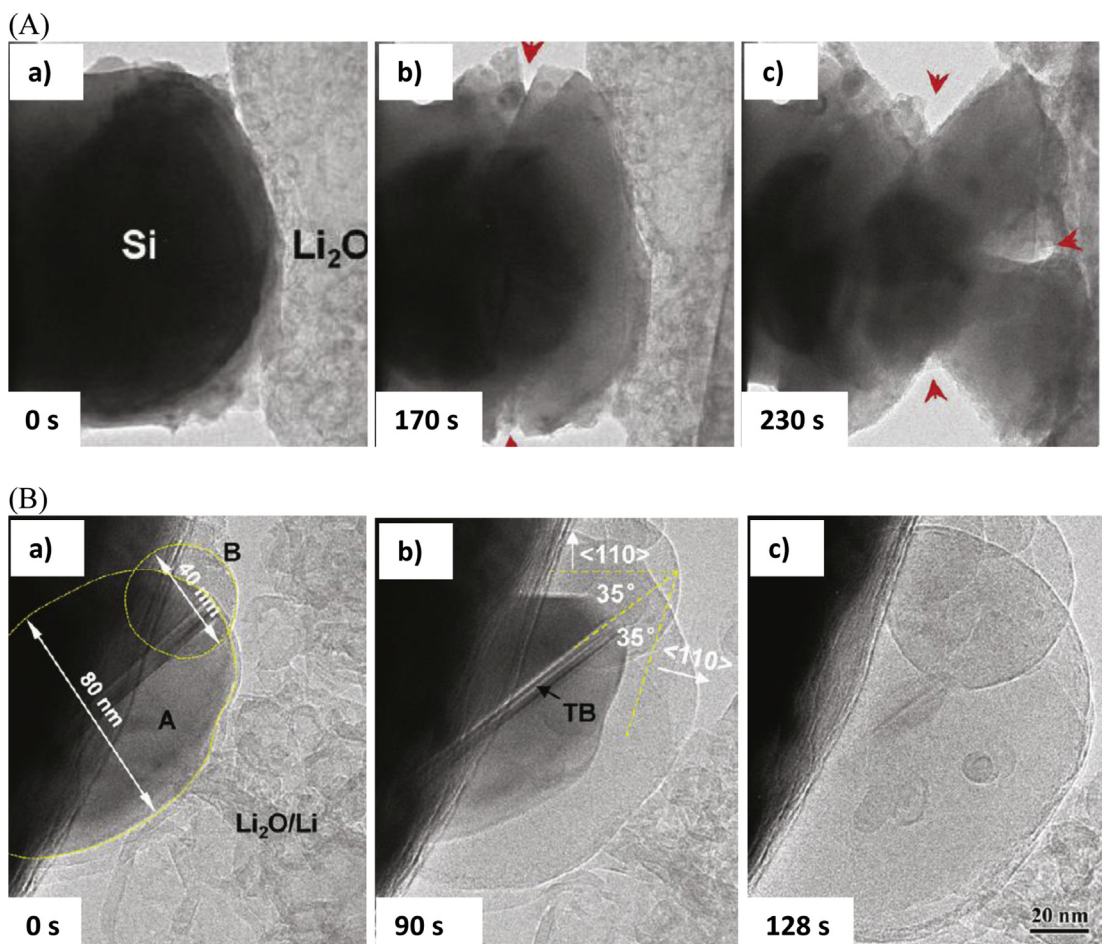


Fig. 7. Surface cracking and fracture of a 960 nm silicon nanoparticle during lithiation (A), and anisotropic lithiation in two smaller particles without cracking. The red arrow in (A) indicating the cracks [81]. (For interpretation of the references to color in this figure legend, the reader is referred to the web version of this article.)

fracture in the surface of any *a*-Si particles with diameters up to 870 nm and the expansion was isotropic during the first lithiation. In addition, unlike *c*-Si particles, a clear concentration boundary that disappeared in the subsequent cycles was observed in *a*-Si particles during the first lithiation. Furthermore, the reaction front did not slow down in the *a*-Si particles during lithiation. These differences imply that the hydrostatic stress in *a*-Si is smaller than that in *c*-Si and Li diffusion is faster in the former. The lack of core-shell structure in the subsequent cycles indicates that the lithiation process changes from two-phase to one-phase. The same lithiation mechanism can also be applied to *c*-Si particles, which become amorphous after the first cycle. These results indicate that amorphous Si materials may undergo more manageable mechanical transformations and are thus more desirable for LIBs.

Even though Ge has a higher cost and lower gravimetric capacity than Si, it has attracted attention owing to its much higher intrinsic electrical conductivity [83–86]. Regardless of the similar volume change, electrochemical behaviors, and products during lithiation/delithiation cycling, Ge and Si show totally different structure evolution during electrochemical cycling. As discussed above, the volume expansion of a Si nanowire is highly anisotropic resulting in a dumbbell-shaped structure, while the expansion of a Ge nanowire is isotropic, as shown in Fig. 8 due to almost the same lithiation rate along different directions. During lithiation/delithiation cycling, instead of cracks, a reversible porous structure is formed in Ge nanowire via a dealloying mechanism [87,88]. The porous structure is quite stable upon cycling indicating the excellent structural integrity of Ge nanowires compared with Si ones.

2.5.1.2. Metal oxides. As discussed in Section 2.3, the first step of lithiation in metal oxides involves an irreversible reaction leading to the formation of metallic particles and amorphous Li_2O matrix, but the details of structure change in the early stage of Li insertion was not clear until the *in situ* TEM technique was applied in the studies of lithiation/delithiation of metal oxides nanostructures [89–92]. Upon lithiation, SnO_2 nanowires underwent elongation

(~60%) and diameter expansion (~45%). In their *in situ* TEM study, Zhong et al. [65] observed interesting multi-stripe lithiation morphology when the SnO_2 nanowire was entirely immersed in the ionic liquid, but not in the one-end contact configuration. The stripes were parallel to the {020} planes of the nanowires. Recently, Nie et al. [93] conducted a systematical study of the structural evaluation during the Li lithiation in SnO_2 nanowires via *in situ* TEM. Surprisingly, they also observed the multi-stripes using the one-end contact setup (Li_2O as the electrolyte), suggesting that the formation of the lithiated stripes is a common characteristic of SnO_2 nanowires, as shown in Fig. 9a. Thus, SnO_2 nanowires were lithiated through a multi-stripe-multi-reaction-front manner instead of a single reaction front. It was found that lithium ions initially preferred to diffuse along the [001] direction in the {200} planes in the SnO_2 crystal forming lithiated strips due to the lowest energy barrier along this direction compared with [110] and [010]. The structure of the lithiated stripes was amorphous due to the Li insertion in the SnO_2 lattices, which also generated dislocations at the tip of the stripes. The structural evolution of SnO_2 nanowires during the lithiation occurs via the initial lithium-ion long-range diffusion inside the pristine SnO_2 lattice along the [001] direction, followed by solid-state amorphization of the nanowire, nucleation of Sn particles, and finally Sn particles alloying into Li_xSn , as summarized in Fig. 9b. Wang et al. [92] found that some of the nanowires were broken into parts after only two cycles. The main reason for the breakdown of nanowires was thermal runaway besides strain induced by lithium insertion, i.e., the nanowires might be melted by the heat generated via charge transport and phase transformation. Further cycling may lead mechanical failure due to the Sn nanoparticle aggregation.

Not all the metal oxides behavior the same way in the lithiation/delithiation process. For example, multi-cracks were formed before

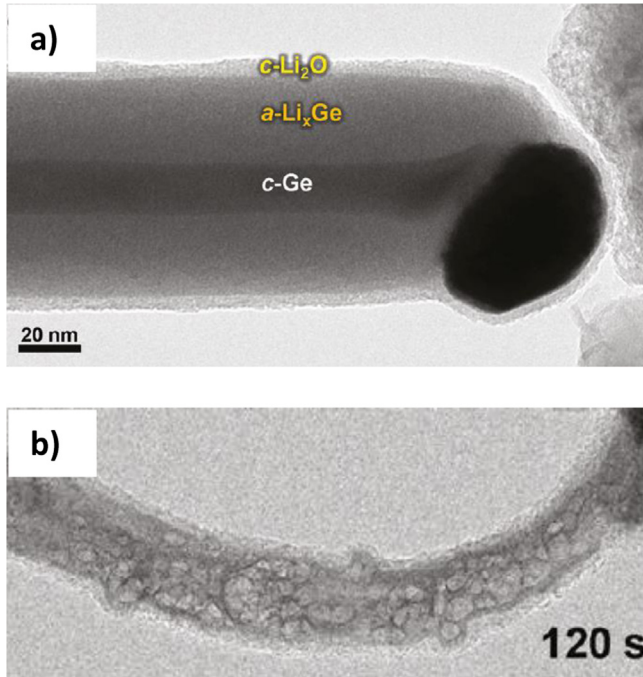


Fig. 8. TEM images showing the intermediate state during isotropic lithiation of a Ge nanowire (a) and porous structure formed after delithiation (b) [87].

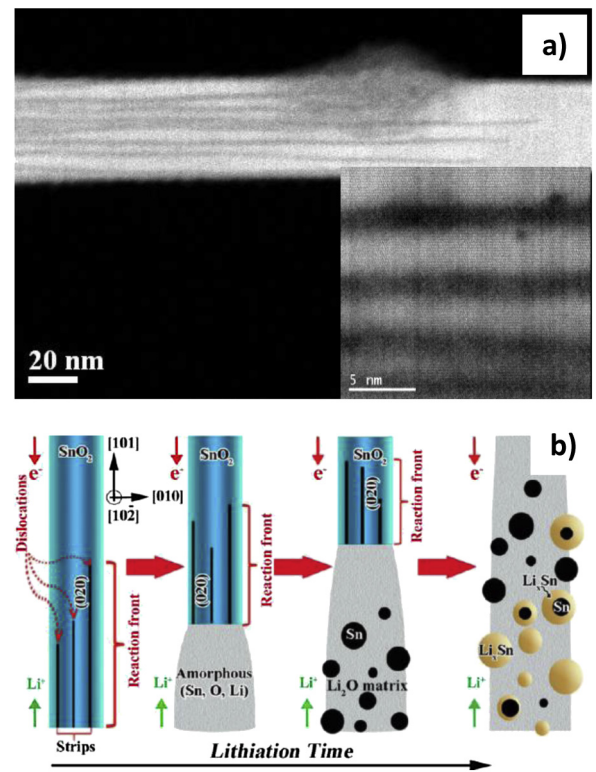


Fig. 9. HADDF image of a SnO_2 nanowire during lithiation showing dark strips parallel to [020] planes (a) and illustration of lithiation process of a SnO_2 nanowire (b). The inset of (a) is a high magnification image of the strips [93].

the reaction front during lithiation of ZnO nanowires [94]. The cracks divided the single-crystalline ZnO nanowire into multiple segments, which were then lithiated individually. The formation of cracks may be the main reason for the much worse cycling capability of ZnO compared with SnO₂.

Various coatings have been explored to suppress the strain and volume expansion induced by lithiation, and to improve the electrical conductivity of SnO₂ nanowires. It was found that both the carbon and copper coatings could effectively suppress the radial expansion, i.e., only elongation was allowed during lithiation [95,96]. In addition, there was no dislocation or stress in the reaction front in all coated nanowires, indicating the role of coatings in strain reduction. It was hypothesized that the Li transport patterns were affected by the coatings, which slowed the Li⁺ diffusion from the interface between the surface and the electrolyte layer to the bulk nanowire in the radial direction.

Metal oxides themselves, especially Al₂O₃ have been used as coatings on both anode and cathode active materials to improve the cyclability of LIBs. The mechanisms of performance were not clear. Liu et al. [97] studied the Al₂O₃ using an Al/Al₂O₃ model system, in which Al nanowires were coated a naturally grown Al₂O₃ surface layer. It was found that the surface Al₂O₃ layer underwent lithiation first forming a Li-Al-O glass layer, followed by the Al nanowire core [97]. The Li-Al-O layer acted as a solid electrolyte in which Li⁺ diffused very fast [98]. The lithiation of the Al nanowire core generated isolated Al nanoparticles, which were encapsulated by a tube defined by the Li-Al-O layer. The formation of a mechanically and chemically robust Li-Al-O glass tube, which preserves the electrical contact and integrity of the active materials and electrodes, is the key to improve the durability of many active materials, such as LiCoO₂ [99–101], LiMn₂O₄ [102–104], LiMn_xNi_yO₂

[105,106], LiV₃O₈ [107], LiNi_{1/3}Co_{1/3}Mn_{1/3} [108,109], and Si [110,111].

2.5.1.3. Carbonaceous materials. The volumetric change and structure degradation of graphite that is the current mostly used anode material is much smaller than that of Si and Sn upon lithiation/delithiation. In addition, given the low mass of Li atoms, the significant radiation damage in the TEM makes the direct imaging of lithiated graphite a challenge [60].

Carbon nanotubes (CNTs) have shown higher capacity than graphite [112–115]. *In situ* TEM results, however, indicated that these materials were not stable and easy to be broken into two pieces during cycling due to the lithiation-induced embrittlement effect [116]. On the other hand, graphene based nanoribbons showed no signs of structural degradation during cycling, suggesting the layered structure was more robust than the tubular ones, such as CNTs [117].

2.5.2. Lithiation and delithiation in cathode materials

Due to less obvious structural and morphological changes during the lithiation/delithiation process of cathode materials, only a few *in situ* TEM studies have been reported so far. Wang et al. [118] conducted a comprehensive study using a semi *in situ* TEM technique to understand the difference in reversibility of lithiation between FeF₂ and CuF₂ particles. The lithiated samples were sealed in a vacuum transfer holder and transferred to the TEM column after they were loaded on the TEM holder without air exposure. Both Fe and Cu nanoparticles formed via the reaction $\text{MF}_2 + 2\text{Li}^+ + 2\text{e}^- \rightarrow 2\text{LiF} + \text{M}$ with no intercalation involved were observed in the TEM images (Fig. 10a and c). Clearly, the Fe nanoparticles were much smaller than Cu and barely visible. The EELS

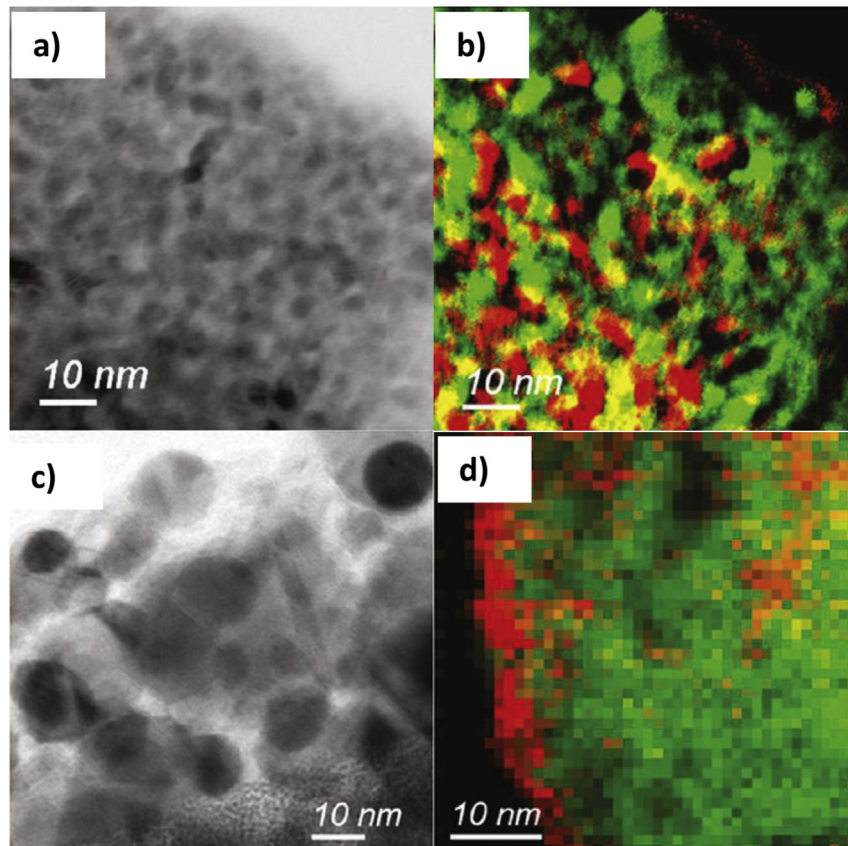


Fig. 10. TEM images (a, c) and EELS mapping (b, d) of FeF₂ and CuF₂ after lithiation [118].

mapping results (Fig. 10b and d) further reveal the morphology difference between these two samples. The Fe nanoparticles were indeed interconnected forming a bicontinuous network, providing a pathway for fast electron transfer, while the large Cu particles were clearly embedded in the LiF matrix and separated from each other. The distinct morphology and phase distribution can be one of the main reasons for the high lithiation reversibility in FeF_2 but poor reversibility in CuF_2 .

In an *in situ* TEM with Li_2O as the solid electrolyte, Zhu and his co-workers [119] for the first time investigated the phase boundary migration at the atomic scale during lithiation of FePO_4 microparticles coated with a 10 nm thick $a\text{-C}$ layer. The anisotropic lithiation in FePO_4 microparticles along the [010] direction was clearly demonstrated, as shown in Fig. 11. The sharp phase boundary between FePO_4 and LiFePO_4 , rather than a solid solution phase, was evidenced by the image contrast and the misfit dislocations along the boundary. The phase boundary moved from the surface toward the core as Li was inserted in the same direction along [010]. The one-dimensional lithiation mechanism caused by the relaxation of the majority of the elastic strain energy is consistent with the theoretical calculations [120–122] and some of the *ex situ* observations [48]. The misfit dislocations formed during lithiation as shown in Fig. 11, are believed to be the origins of the preferential sites for cracking. It is worth noting that the lithiation mechanism may depend on the size of FePO_4 particles. The one-dimensional lithiation process may not occur in FePO_4 nanoparticles as the Li^+ diffusivity in nanoparticles is much higher than that in microparticles and a coherent phase boundary is preferable.

3. Summary

Compared with other characterization techniques, microscopies have many advantages due to their abilities of directly (or indirectly) recording the morphological and microstructural changes of battery electrodes and active materials. By combining with other spectroscopic techniques, such as XAS and EELS, they are also able to map the charge distribution in the electrode or even within a particle. These results are particularly critical for understanding the charge/discharge mechanisms in the active materials. Another advantage of microscopic techniques is that all the morphological/structural changes and charge distributions can be studied under potential control in a battery (or mimic) environment, which is very important because the lithiated materials are very sensitive to air and moisture.

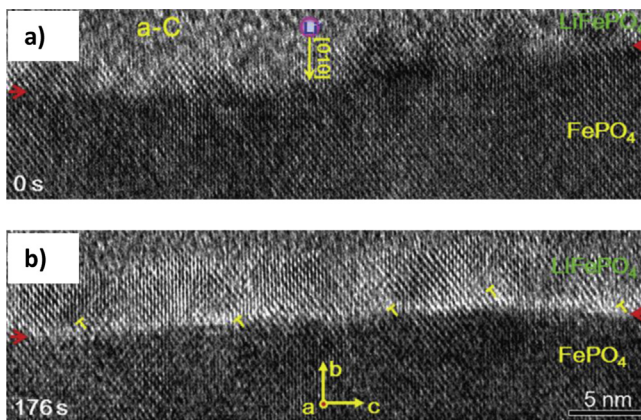


Fig. 11. TEM images showing migration of phase boundary between LiFePO_4 and FePO_4 along the [010] direction during lithiation. The initial state right after re-turning the electron beam showing the clear phase boundary (a) and after 176 s of lithiation (b). The FePO_4 was coated with a 10 nm thick $a\text{-C}$ layer. The invert "T" marks the mismatch dislocations in the phase boundary [119].

Table 1

Comparisons of different microscopic techniques and their suitable applications in the study of LIB materials.

<i>In situ</i> microscopic techniques	Spatial resolution	Suitable for			
		Large morphology change	Subtle morphology change	Li diffusion interface	Charge distribution
XRF	~ μm	Y	N	N	N
Raman	Hundreds of nm	Y	N	N	Y
STXM	~30 nm	Y	N	N	Y
SEM	~nm	Y	Y	N	N
TEM	Atomic	Y	Y	Y	Y

Depending on the nature of the problem, proper microscopic techniques should be chosen based on their properties, as summarized in Table 1. The spatial resolutions increase from $\sim\mu\text{m}$ for XRF to sub-nanometer for TEM. As a result, XRF, Raman, and STXM cannot reveal subtle morphological changes due to their low spatial resolutions, while only TEM is able to identify the boundaries of phase transformation during lithiation/delithiation if there is any. On the other hand, compared with SEM and TEM, the advantages of XRF, Raman, and STXM are that these measurements can be conducted with real battery electrodes and electrolytes. In SEM and TEM, however, due to the requirement of an extra high vacuum, compromises such as using ionic liquid and solid electrolytes have to be made in order to achieve a high spatial resolution. In addition, it is almost impossible to measure the faradic current due to limited electrons passing through the nanobattery and large internal resistances in the open cell design of *in situ* TEM. As a result, the direct correlation between the structural change and the charge states of the active materials is difficult. Even for TEM, the direct imaging of Li columns with atomic resolution in real time remains a considerable challenge. Nevertheless, *in situ* TEM techniques have become a powerful tool to monitor in real time the morphological changes of active materials, especially for anode materials, which undergo significant volume changes during charging/discharging. However, there are only a couple of reports in the study of cathode materials due to their subtle structural changes compared with anode materials. By combining with EELS techniques to identify oxide states and charge distributions, *in situ* TEM may expand its applications in the study of cathode materials and even the solid electrolyte interlayer (SEI) [64].

Acknowledgment

This work was supported by the start-up fund from the Hong Kong University of Science and Technology.

References

- J.M. Tarascon, Philos. Trans. R. Soc. A Math. Phys. Eng. Sci. 368 (2010) 3227–3241.
- J.B. Goodenough, Y. Kim, Chem. Mater. 22 (2010) 587–603.
- B. Kang, G. Ceder, Nature 458 (2009) 190–193.
- J.M. Tarascon, M. Armand, Nature 414 (2001) 359–367.
- Y.-K. Sun, S.-T. Myung, B.-C. Park, J. Prakash, I. Belharouak, K. Amine, Nat. Mater. 8 (2009) 320–324.
- A. Kraytsberg, Y. Ein-Eli, Adv. Energy Mater. 2 (2012) 922–939.
- J. Chen, Materials 6 (2013) 156–183.
- J.T. Li, J.C. Fang, H. Su, S.G. Sun, Prog. Chem. 23 (2011) 349–356.
- W.S. Yoon, M. Balasubramanian, K.Y. Chung, X.Q. Yang, J. McBreen, C.P. Grey, D.A. Fischer, J. Am. Chem. Soc. 127 (2005) 17479–17487.
- W.-S. Yoon, K.Y. Chung, J. McBreen, X.-Q. Yang, Electrochim. Commun. 8 (2006) 1257–1262.
- J. Li, J.R. Dahn, J. Electrochem. Soc. 154 (2007) A156–A161.
- L.J. Hardwick, P.W. Ruch, M. Hahn, W. Scheifele, R. Koetz, P. Novak, J. Phys. Chem. Solids 69 (2008) 1232–1237.

[13] B.R. Long, M.K.Y. Chan, J.P. Greeley, A.A. Gewirth, *J. Phys. Chem. C* 115 (2011) 18916–18921.

[14] B. Key, M. Morcrette, J.-M. Tarascon, C.P. Grey, *J. Am. Chem. Soc.* 133 (2011) 503–512.

[15] R. Bhattacharyya, B. Key, H. Chen, A.S. Best, A.F. Hollenkamp, C.P. Grey, *Nat. Mater.* 9 (2010) 504–510.

[16] R. Robert, D. Zeng, A. Lanzirotti, P. Adamson, S.J. Clarke, C.P. Grey, *Chem. Mater.* 24 (2012) 2684–2691.

[17] T. Nishi, H. Nakai, A. Kita, *J. Electrochem. Soc.* 160 (2013) A1785–A1788.

[18] S.-C. Chao, Y.-F. Song, C.-C. Wang, H.-S. Sheu, H.-C. Wu, N.-L. Wu, *J. Phys. Chem. C* 115 (2011) 22040–22047.

[19] D. Chen, S. Indris, M. Schulz, B. Gumer, R. Möning, *J. Power Sources* 196 (2011) 6382–6387.

[20] X.H. Liu, J.Y. Huang, *Energy Environ. Sci.* 4 (2011) 3844–3860.

[21] X.H. Liu, Y. Liu, A. Kushima, S. Zhang, T. Zhu, J. Li, J.Y. Huang, *Adv. Energy Mater.* 2 (2012) 722–741.

[22] A.E. Semenov, I.N. Borodina, S.H. Garofalini, *J. Electrochem. Soc.* 148 (2001) A1239–A1246.

[23] Sanjay Ramdon, B. Bhushan, S.C. Nagpure, *J. Power Sources* 249 (2014) 373–384.

[24] F.M.F. de Groot, E. de Smit, M.M. van Schooneveld, L.R. Aramburo, B.M. Weckhuysen, *ChemPhysChem* 11 (2010) 951–962.

[25] M. West, A.T. Ellis, P.J. Potts, C. Streli, C. Vanhoof, D. Wegrzynek, P. Wobrauschek, *J. Anal. Atom. Spectrom.* 28 (2013) 1544–1590.

[26] Z.A. Gál, O.J. Rutt, C.F. Smura, T.P. Overton, N. Barrier, S.J. Clarke, J. Hadermann, *J. Am. Chem. Soc.* 128 (2006) 8530–8540.

[27] O.J. Rutt, G.R. Williams, S.J. Clarke, *Chem. Commun.* (2006) 2869–2871.

[28] R. Baddour-Hadjean, J.-P. Pereira-Ramos, *Chem. Rev.* 110 (2009) 1278–1319.

[29] J.-C. Panitz, P. Novák, *J. Power Sources* 97–98 (2001) 174–180.

[30] J. Lei, F. McLarnon, R. Kostecki, *J. Phys. Chem. B* 109 (2004) 952–957.

[31] R. Kostecki, F. McLarnon, *Electrochim. Solid-State Lett.* 7 (2004) A380–A383.

[32] M. Kerlau, M. Marcinek, V. Srinivasan, R.M. Kostecki, *Electrochim. Acta* 53 (2007) 1385–1392.

[33] J. Nanda, J. Remillard, A. O'Neill, D. Bernardi, T. Ro, K.E. Nietering, J.-Y. Go, T.J. Miller, *Adv. Funct. Mater.* 21 (2011) 3282–3290.

[34] Q. Shi, Y. Takahashi, J. Akimoto, I.C. Stefan, D.A. Scherson, *Electrochim. Solid-State Lett.* 8 (2005) A521–A524.

[35] D. Guay, J. Stewart-Ornstein, X. Zhang, A.P. Hitchcock, *Anal. Chem.* 77 (2005) 3479–3487.

[36] Y.-C.K. Chen-Wiegert, Z. Liu, K.T. Faber, S.A. Barnett, J. Wang, *Electrochim. Commun.* 28 (2013) 127–130.

[37] J. Wang, Y.-C. Karen Chen, Q. Yuan, A. Tkachuk, C. Erdonmez, B. Hornberger, M. Feser, *Appl. Phys. Lett.* 100 (2012).

[38] J. Nelson, S. Misra, Y. Yang, A. Jackson, Y. Liu, H. Wang, H. Dai, J.C. Andrews, Y. Cui, M.F. Toney, *J. Am. Chem. Soc.* 134 (2012) 6337–6343.

[39] Florian Meirer, Jordi Cabana, Yijin Liu, Apurva Mehta, Joy C. Andrews, P. Pianettac, J. Synchrotron Radiat. 18 (2011) 773–781.

[40] M. Ebner, F. Geldmacher, F. Marone, M. Stampanoni, V. Wood, *Adv. Energy Mater.* 3 (2013) 845–850.

[41] M. Jiang, B. Lim, J. Tao, P.H.C. Camargo, C. Ma, Y. Zhu, Y. Xia, *Nanoscale* 2 (2010) 2406–2411.

[42] S.-C. Chao, Y.-C. Yen, Y.-F. Song, H.-S. Sheu, H.-C. Wu, N.-L. Wu, *J. Electrochim. Soc.* 158 (2011) A1335–A1339.

[43] J. Wang, Y.-C.K. Chen-Wiegert, J. Wang, *Chem. Commun.* 49 (2013) 6480–6482.

[44] W. Chao, P. Fischer, T. Tyliszczak, S. Rekawa, E. Anderson, P. Naulleau, *Opt. Exp.* 20 (2012) 9777–9783.

[45] K.B. Burke, A.J. Stapleton, B. Vaughan, X. Zhou, A.L.D. Kilcoyne, W.J. Belcher, P.C. Dastoor, *Nanotechnology* 22 (2011) 265710.

[46] W.C. Chueh, F. El Gabaly, J.D. Sugar, N.C. Bartelt, A.H. McDaniel, K.R. Fenton, K.R. Zavadil, T. Tyliszczak, W. Lai, K.F. McCarty, *Nano Lett.* 13 (2013) 866–872.

[47] L. Laffont, C. Delacourt, P. Gibot, M.Y. Wu, P. Kooyman, C. Masquelier, J.M. Tarascon, *Chem. Mater.* 18 (2006) 5520–5529.

[48] G.Y. Chen, X.Y. Song, T.J. Richardson, *Electrochim. Solid-State Lett.* 9 (2006) A295–A298.

[49] U. Boessenberg, F. Meirer, Y. Liu, A.K. Shukla, R. Dell'Anna, T. Tyliszczak, G. Chen, J.C. Andrews, T.J. Richardson, R. Kostecki, J. Cabana, *Chem. Mater.* 25 (2013) 1664–1672.

[50] J. Zhou, J. Wang, Y. Hu, T. Regier, H. Wang, Y. Yang, Y. Cui, H. Dai, *Chem. Commun.* 49 (2013) 1765–1767.

[51] D. Aurbach, Y. Gofer, J. Langzam, *J. Electrochim. Soc.* 136 (1989) 3198–3205.

[52] P. Baudry, M. Armand, *Solid State Ionics* 28–30 (1988) 1567–1571.

[53] F. Orsini, A. Du Pasquier, B. Beaudoin, J.M. Tarascon, M. Trentin, N. Langenhuijsen, E. De Beer, P. Notten, *J. Power Sources* 76 (1998) 19–29.

[54] R. Huang, T. Hitosugi, S.D. Findlay, C.A.J. Fisher, Y.H. Ikuhara, H. Moriwake, H. Oki, Y. Ikuhara, *Appl. Phys. Lett.* 98 (2011).

[55] S.D. Findlay, N.R. Lugg, N. Shibata, L.J. Allen, Y. Ikuhara, *Ultramicroscopy* 111 (2011) 1144–1154.

[56] S. Lee, Y. Oshima, H. Sawada, F. Hosokawa, E. Okunishi, T. Kaneyama, Y. Kondo, S. Niitaka, H. Takagi, Y. Tanishiro, K. Takayanagi, *J. Appl. Phys.* 109 (2011).

[57] Y. Oshima, H. Sawada, F. Hosokawa, E. Okunishi, T. Kaneyama, Y. Kondo, S. Niitaka, H. Takagi, Y. Tanishiro, K. Takayanagi, *J. Electron Microsc.* 59 (2010) 457–461.

[58] Y. Shao-Horn, L. Croguennec, C. Delmas, E.C. Nelson, M.A. O'Keefe, *Nat. Mater.* 2 (2003) 464–467.

[59] X.Y. Song, K. Kinoshita, T.D. Tran, *J. Electrochim. Soc.* 143 (1996) L120–L123.

[60] F. Wang, J. Graetz, M.S. Moreno, C. Ma, L. Wu, V. Volkov, Y. Zhu, *ACS Nano* 5 (2011) 1190–1197.

[61] H. Gabrisch, R. Yazami, B. Fultz, *Electrochim. Solid-State Lett.* 5 (2002) A111–A114.

[62] S.W. Lee, M.T. McDowell, J.W. Choi, Y. Cui, *Nano Lett.* 11 (2011) 3034–3039.

[63] M. Gu, L.R. Parent, B.L. Mehdi, R.R. Unocic, M.T. McDowell, R.L. Sacci, W. Xu, J.G. Connell, P. Xu, P. Abellan, X. Chen, Y. Zhang, D.E. Perea, J.E. Evans, L.J. Lauhon, J.-G. Zhang, J. Liu, N.D. Browning, Y. Cui, I. Arslan, C.-M. Wang, *Nano Lett.* 13 (2013) 6106–6112.

[64] R.R. Unocic, in: *DOE Vehicle Technologies Program Annual Merit Review*, 2013. Washington DC.

[65] L. Zhong, X.H. Liu, G.F. Wang, S.X. Mao, J.Y. Huang, *Phys. Rev. Lett.* 106 (2011).

[66] L. Baggetto, P.H.L. Notten, *J. Electrochim. Soc.* 156 (2009) A169–A175.

[67] D. Larcher, S. Beattie, M. Morcrette, K. Edstroem, J.-C. Jumas, J.-M. Tarascon, *J. Mater. Chem.* 17 (2007) 3759–3772.

[68] H. Wu, Y. Cui, *Nano Today* 7 (2012) 414–429.

[69] X.H. Liu, H. Zheng, L. Zhong, S. Huan, K. Karki, L.Q. Zhang, Y. Liu, A. Kushima, W.T. Liang, J.W. Wang, J.-H. Cho, E. Epstein, S.A. Dayeh, S.T. Picraux, T. Zhu, J. Li, J.P. Sullivan, J. Cumings, C. Wang, S.X. Mao, Z.Z. Ye, S. Zhang, J.Y. Huang, *Nano Lett.* 11 (2011) 3312–3318.

[70] M.K.Y. Chan, B.R. Long, A.A. Gewirth, J.P. Greeley, *J. Phys. Chem. Lett.* 2 (2011) 3092–3095.

[71] M. Gu, Z. Wang, J.G. Connell, D.E. Perea, L.J. Lauhon, F. Gao, C. Wang, *ACS Nano* 7 (2013) 6303–6309.

[72] C.-M. Wang, X. Li, Z. Wang, W. Xu, J. Liu, F. Gao, L. Kovarik, J.-G. Zhang, J. Howe, D.J. Burton, Z. Liu, X. Xiao, S. Thevuthasan, D.R. Baer, *Nano Lett.* 12 (2012) 1624–1632.

[73] X.H. Liu, L.Q. Zhang, L. Zhong, Y. Liu, H. Zheng, J.W. Wang, J.-H. Cho, S.A. Dayeh, S.T. Picraux, J.P. Sullivan, S.X. Mao, Z.Z. Ye, J.Y. Huang, *Nano Lett.* 11 (2011) 2251–2258.

[74] L.-F. Cui, R. Ruffo, C.K. Chan, H. Peng, Y. Cui, *Nano Lett.* 9 (2009) 491–495.

[75] R. Huang, X. Fan, W. Shen, J. Zhu, *Appl. Phys. Lett.* 95 (2009).

[76] T. Ishihara, M. Nakasu, M. Yoshi, H. Nishiguchi, Y. Takita, *J. Power Sources* 146 (2005) 161–165.

[77] S.-H. Ng, J. Wang, D. Wexler, K. Konstantinov, Z.-P. Guo, H.-K. Liu, *Angew. Chem. Int. Ed.* 45 (2006) 6896–6899.

[78] J.W. Wang, X.H. Liu, K. Zhao, A. Palmer, E. Patten, D. Burton, S.X. Mao, Z. Suo, J.Y. Huang, *ACS Nano* 6 (2012) 9158–9167.

[79] K. Karki, E. Epstein, J.-H. Cho, Z. Jia, T. Li, S.T. Picraux, C. Wang, J. Cumings, *Nano Lett.* 12 (2012) 1392–1397.

[80] H. Kim, M. Seo, M.-H. Park, J. Cho, *Angew. Chem. Int. Ed.* 49 (2010) 2146–2149.

[81] X.H. Liu, L. Zhong, S. Huang, S.X. Mao, T. Zhu, J.Y. Huang, *ACS Nano* 6 (2012) 1522–1531.

[82] M.T. McDowell, I. Ryu, S.W. Lee, C. Wang, W.D. Nix, Y. Cui, *Adv. Mater.* 24 (2012) 6034–6041.

[83] M.-H. Park, K. Kim, J. Kim, J. Cho, *Adv. Mater.* 22 (2010) 415–418.

[84] B. Laforge, L. Levan-Jodin, R. Salot, A. Billard, *J. Electrochim. Soc.* 155 (2008) A181–A188.

[85] K.H. Seng, M.-H. Park, Z.P. Guo, H.K. Liu, J. Cho, *Angew. Chem. Int. Ed.* 51 (2012) 5657–5661.

[86] L.C. Yang, Q.S. Gao, L. Li, Y. Tang, Y.P. Wu, *Electrochim. Commun.* 12 (2010) 418–421.

[87] X.H. Liu, S. Huang, S.T. Picraux, J. Li, T. Zhu, J.Y. Huang, *Nano Lett.* 11 (2011) 3991–3997.

[88] M.-H. Park, Y. Cho, K. Kim, J. Kim, M. Liu, J. Cho, *Angew. Chem. Int. Ed.* 50 (2011) 9647–9650.

[89] J.Y. Huang, L. Zhong, C.M. Wang, J.P. Sullivan, W. Xu, L.Q. Zhang, S.X. Mao, N.S. Hudak, X.H. Liu, A. Subramanian, H. Fan, L. Qi, A. Kushima, J. Li, *Science* 330 (2010) 1515–1520.

[90] L.Q. Zhang, X.H. Liu, Y.-C. Perng, J. Cho, J.P. Chang, S.X. Mao, Z.Z. Ye, J.Y. Huang, *Micron* 43 (2012) 1127–1133.

[91] S.P. Hsu, C.W. Liu, H.S. Chen, T.Y. Chen, C.M. Lai, C.H. Lee, J.F. Lee, T.S. Chan, L.D. Tsai, K.W. Wang, *Electrochim. Acta* 105 (2013) 180–187.

[92] L. Wang, Z. Xu, S. Yang, X. Tian, J. Wei, W. Wang, X. Bai, *Sci. China Technol. Sci.* 56 (2013) 2630–2635.

[93] A. Nie, L.-Y. Gan, Y. Cheng, H. Asayesh-Ardakani, Q. Li, C. Dong, R. Tao, F. Mashayek, H.-T. Wang, U. Schwingenschlögl, R.F. Kliew, R.S. Yassar, *ACS Nano* 7 (2013) 6203–6211.

[94] A. Kushima, X.H. Liu, G. Zhu, Z.L. Wang, J.Y. Huang, J. Li, *Nano Lett.* 11 (2011) 4535–4541.

[95] L.Q. Zhang, X.H. Liu, Y. Liu, S. Huang, T. Zhu, L. Gui, S.X. Mao, Z.Z. Ye, C.M. Wang, J.P. Sullivan, J.Y. Huang, *ACS Nano* 5 (2011) 4800–4809.

[96] Y.-S. Lin, J.-G. Duh, M.-H. Hung, J. *Phys. Chem. C* 114 (2010) 13136–13141.

[97] Y. Liu, N.S. Hudak, D.L. Huber, S.J. Limmer, J.P. Sullivan, J.Y. Huang, *Nano Lett.* 11 (2011) 4188–4194.

[98] S.C. Jung, Y.-K. Han, *J. Phys. Chem. Lett.* 4 (2013) 2681–2685.

[99] I.D. Scott, Y.S. Jung, A.S. Cavanagh, Y. An, A.C. Dillon, S.M. George, S.-H. Lee, *Nano Lett.* 11 (2011) 414–418.

[100] J. Cho, Y.J. Kim, B. Park, *Chem. Mater.* 12 (2000) 3788–3791.

[101] H.-M. Cheng, F.-M. Wang, J.P. Chu, R. Santhanam, J. Rick, S.-C. Lo, *J. Phys. Chem. C* 116 (2012) 7629–7637.

[102] T.-F. Yi, Y.-R. Zhu, X.-D. Zhu, J. Shu, C.-B. Yue, A.-N. Zhou, *Ionics* 15 (2009) 779–784.

[103] J. Zhao, Y. Wang, *J. Solid State Electrochem.* 17 (2013) 1049–1058.

[104] D. Guan, J.A. Jeevarajan, Y. Wang, *Nanoscale* 3 (2011) 1465–1469.

[105] X. Fang, M. Ge, J. Rong, Y. Che, N. Aroonyadet, X. Wang, Y. Liu, A. Zhang, C. Zhou, *Energy Technol.* 2 (2014) 159–165.

[106] X. Xiao, D. Ahn, Z. Liu, J.-H. Kim, P. Lu, *Electrochem. Commun.* 32 (2013) 31–34.

[107] S. Huang, J.P. Tu, X.M. Jian, Y. Lu, S.J. Shi, X.Y. Zhao, T.Q. Wang, X.L. Wang, C.D. Gu, *J. Power Sources* 245 (2014) 698–705.

[108] X. Li, W. He, L. Chen, W. Guo, J. Chen, Z. Xiao, *Ionics* (2013) 1–8.

[109] Y. Huang, J. Chen, F. Cheng, W. Wan, W. Liu, H. Zhou, X. Zhang, *J. Power Sources* 195 (2010) 8267–8274.

[110] H.T. Nguyen, M.R. Zamfir, L.D. Duong, Y.H. Lee, P. Bondavalli, D. Pribat, *J. Mater. Chem.* 22 (2012) 24618–24626.

[111] J. Li, X. Xiao, Y.-T. Cheng, M.W. Verbrugge, *J. Phys. Chem. Lett.* 4 (2013) 3387–3391.

[112] B.J. Landi, M.J. Ganter, C.D. Cress, R.A. DiLeo, R.P. Raffaele, *Energy Environ. Sci.* 2 (2009) 638–654.

[113] Y.P. Wu, E. Rahm, R. Holze, *J. Power Sources* 114 (2003) 228–236.

[114] B. Gao, A. Kleinhammes, X.P. Tang, C. Bower, L. Fleming, Y. Wu, O. Zhou, *Chem. Phys. Lett.* 307 (1999) 153–157.

[115] I. Lahiri, S.-W. Oh, J.Y. Hwang, S. Cho, Y.-K. Sun, R. Banerjee, W. Choi, *ACS Nano* 4 (2010) 3440–3446.

[116] Y. Liu, H. Zheng, X.H. Liu, S. Huang, T. Zhu, J. Wang, A. Kushima, N.S. Hudak, X. Huang, S. Zhang, S.X. Mao, X. Qian, J. Li, J.Y. Huang, *ACS Nano* 5 (2011) 7245–7253.

[117] X.H. Liu, J.W. Wang, Y. Liu, H. Zheng, A. Kushima, S. Huang, T. Zhu, S.X. Mao, J. Li, S. Zhang, W. Lu, J.M. Tour, J.Y. Huang, *Carbon* 50 (2012) 3836–3844.

[118] F. Wang, R. Robert, N.A. Chernova, N. Pereira, F. Badway, X. Hua, M. Ruotolo, R. Zhang, L. Wu, V. Volkov, D. Su, B. Key, M.S. Whittingham, C.P. Grey, G.G. Amatucci, Y. Zhu, J. Graetz, *J. Am. Chem. Soc.* 133 (2011) 18828–18836.

[119] Y. Zhu, J.W. Wang, Y. Liu, X. Liu, A. Kushima, Y. Liu, Y. Xu, S.X. Mao, J. Li, C. Wang, J.Y. Huang, *Adv. Mater.* 25 (2013) 5461–5466.

[120] J.L. Allen, T.R. Jow, J. Wolfenstine, *Chem. Mater.* 19 (2007) 2108–2111.

[121] M.S. Islam, D.J. Driscoll, C.A.J. Fisher, P.R. Slater, *Chem. Mater.* 17 (2005) 5085–5092.

[122] D. Morgan, A. Van der Ven, G. Ceder, *Electrochim. Solid State Lett.* 7 (2004) A30–A32.